Simulation of thermal effects in optoelectronic devices using coupled energy-transport and circuit models*

Markus Brunk

Institut für Mathematik, Universität Mainz, Staudingerweg 9, 55099 Mainz, Germany; brunk@mathematik.uni-mainz.de

Ansgar Jüngel

Institut für Analysis und Scientific Computing, Technische Universität Wien, Wiedner Hauptstr. 8-10, 1040 Wien, Austria; juengel@anum.tuwien.ac.at

Received (Day Month Year)
Revised (Day Month Year)
Communicated by (xxxxxxxxxx)

A coupled model with optoelectronic semiconductor devices in electric circuits is proposed. The circuit is modeled by differential-algebraic equations derived from modified nodal analysis. The transport of charge carriers in the semiconductor devices (laser diode and photo diode) is described by the energy-transport equations for the electron density and temperature, the drift-diffusion equations for the hole density, and the Poisson equation for the electric potential. The generation of photons in the laser diode is modeled by spontaneous and stimulated recombination terms appearing in the transport equations. The devices are coupled to the circuit by the semiconductor current entering the circuit and by the applied voltage at the device contacts, coming from the circuit. The resulting time-dependent model is a system of nonlinear partial differential-algebraic equations. The one-dimensional transient transport equations are numerically discretized in time by the backward Euler method and in space by a hybridized mixed finite-element method. Numerical results for a circuit consisting of a single-mode heterostructure laser diode, a silicon photo diode, and a high-pass filter are presented.

Keywords: Laser diode, photo diode, electric circuits, energy-transport equations, drift-diffusion equations, partial differential-algebraic equations, mixed finite-element method, high-pass filter.

AMS Subject Classification: 78A35, 82D37, 65M60, 65L80.

*The authors acknowledge partial support from the German Federal Ministry of Education and Research (BMBF), grant 03JUNAVN. The second author has been partially supported by the FWF Wissenschaftskolleg "Differential equations". This research is part of the ESF program "Global and geometrical aspects of nonlinear partial differential equations (GLOBAL)". The authors thank Dr. Carlo de Falco and Dr. Uwe Feldmann (Qimonda, Munich) for fruitful discussions.

1. Introduction

Semiconductor lasers are important devices in optoelectronic integrated circuits for high-speed communication systems. First phenomenological approaches to model laser diodes consisted in a direct relation between the driving current and the output power.[10] Increasingly complex device structures made it necessary to include semiconductor device equations for better accuracy. In Refs. 4 and 27, for instance, the drift-diffusion equations are employed to model the charge transport in the device, coupled with an appropriate model for the optical effects.

Thermal effects play an important role in laser diodes and have to be included in the mathematical models. By considering an equivalent thermal circuit, a linear second-order equation for the laser temperature has been derived in Ref. 3. Temperature-dependent models are also included in the commercial laser diode simulators LASTIP and PICS3D which are based on the drift-diffusion model.[12] A heat flux equation for the lattice temperature was recently derived in Ref. 5 from a thermodynamics-based model.

The objective of this paper is the numerical simulation of thermal effects in laser and photo diodes which are part of an electric circuit. The thermal effects are modeled by the energy-transport equations for the electron temperature, derived from the semiconductor Boltzmann equation.[7,13] The electric circuit is described by differential-algebraic equations derived from modified nodal analysis.[14,31] We simulate for the first time a coupled optoelectronic device-circuit model by using the semiconductor energy-transport equations.

In the following we describe some models for optical effects in photonic devices used in the literature. The optical effects in the laser diode can be modeled by a rate equation for the number of photons. In Refs. 1 (§6.2) and 32, the intensity of the optical field confined to the active region is approximated by the so-called confinement factor. However, this does not allow for a local coupling between the electrical and optical effects. The model can be improved by replacing the confinement factor by the local intensity distribution computed from the waveguide equation.[4] Further improvements are obtained by considering several rate equations for each laser mode and by including quantum effects.[4] Another possibility to increase the accuracy of the models is to decompose the optical field inside the laser into forward and backward propagating waves whose amplitudes are calculated from the travelling wave equation.[6,21] Also in this approach, thermal effects may be included.[23]

Photo diodes can be described by equivalent circuit models[30] or drift-diffusion equations,[20] where the optical effects are taken into account by a generation term.[11,17] Since the drift-diffusion equations cannot capture thermal effects in the device, we employ in this paper the energy-transport equations for the electron transport.

The model studied in this paper consists of the energy-transport equations for the electron density and the particle temperature and the drift-diffusion equations for the hole density, coupled to the Poisson equation for the electric potential. The

generation of photons in the laser diode is modeled by spontaneous and stimulated emission terms in the transport equations. The stimulated emission is assumed to be proportional to the number of photons, which is balanced by a rate equation, and to the intensity distribution, which is computed from the eigenvalue problem of the waveguide equation or from the effective index approximation (see Ref. 1, Chap. 2.5). The generation of electrons in the photo diode is described by a generation term depending on the power of the irradiation. Finally, the nonlinear partial differential equations (PDE) resulting from the device model are coupled to the differential-algebraic equations (DAE) of the electric circuit. The complete model becomes a system of nonlinear partial differential-algebraic equations. We remark that such systems have been studied mathematically and numerically only recently.[2,28]

The one-dimensional transient energy-transport equations are numerically discretized in time by the implicit Euler method and in space by exponentially fitted hybrid-mixed finite elements. The use of the Marini-Pietra finite elements[24] guarantees the positivity of the electron and hole densities for positive Dirichlet boundary data. As suggested in Ref. 8, we employ Robin boundary conditions for the particle and energy densities in order to reduce boundary layers in the bipolar devices. We are able to show that the positivity property still holds in the case of Robin boundary conditions. The discrete system of equations is solved by a variant of the Gummel method combined with a continuation method in the applied voltage. The nonlinear DAE system of the circuit is solved by Newton's method, and the coupled system (PDE and DAE) is solved iteratively.

We present numerical results for a single-mode $Al_{0.7}Ga_{0.3}As$/GaAs laser diode and a silicon photo diode. The results obtained from the energy-transport model are compared with those computed from the drift-diffusion equations. Moreover, a high-pass filter with a photo diode and a laser diode is simulated. The numerical results show that thermal effects are significant for large applied bias.

2. Modeling

2.1. *Laser diode*

As a simplified model of a laser diode we consider a heterostructure *p*-*i*-*n* diode as displayed in Figure 1. It consists of an intrinsic or lowly doped part of a low band-gap semiconductor material like GaAs sandwiched by highly doped cladding layers made from a semiconductor material with a higher band-gap like $Al_{0.7}Ga_{0.3}As$. The different band gaps of the heterostructure result in a bending of the energy bands (see Ref. 27, §3.3, and Ref. 11). Due to the lower band gap the charge carriers tend to move to the intrinsic region as this corresponds to a state of lower energy, causing carrier confinement. For a forward biased device the number of free charge carriers increases and spontaneous and stimulated emission of photons occurs due to recombination effects. Thus, an optical field represented by photons arises in the intrinsic region and, as the facets of the device are polished, the intrinsic region works as a laser cavity or a simple Fabry-Perot laser.[4]

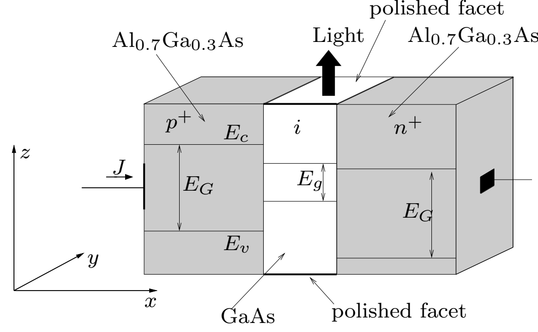

Fig. 1. Simplified structure of a laser diode including a schematic illustration of the energy bands before assembling the different materials. Here, E_c denotes the conduction band energy, E_v the valence band energy, and E_G and E_g the energy gaps of the corresponding materials.

Transport equations. In the device, we assume that the electron flow is described by the energy-transport equations.[18] They consist of the (scaled) conservation laws for the particle density n and energy density w,

$$\partial_t n - \mathrm{div} J_n = -R(n,p), \tag{2.1}$$

$$\partial_t w - \mathrm{div} J_w = -J_n \cdot \nabla V_n + W(n,T) - \frac{3}{2} T R(n,p), \tag{2.2}$$

together with (scaled) constitutive relations for the particle current density J_n and the energy current density J_w,

$$J_n = \mu_n \Big(\nabla n - \frac{n}{T} \nabla V_n \Big), \quad J_w = \frac{3}{2} \mu_n (\nabla(nT) - n \nabla V_n). \tag{2.3}$$

Here, the electron temperature T is defined by the relation $w = \frac{3}{2} nT$, and the effective potential $V_n = V + U_n$ is given as the sum of the electric potential V and the band potential U_n. The band potential is a simple model of the carrier confinement caused by the difference of the material band gaps. It is positive within the active intrinsic region and zero outside.

The transport equations are solved in a bounded domain $\Omega \subset \mathbb{R}^d$ ($d \geq 1$) and are coupled self-consistently to the Poisson equation for the electric potential V,

$$\lambda^2 \Delta V = n - p - C(x), \tag{2.4}$$

where $C(x)$ models fixed charged background ions (doping profile) and p denotes the hole density determined by the drift-diffusion equations,

$$\partial_t p + \mathrm{div} J_p = -R(n,p), \quad J_p = -\mu_p (\nabla p + p \nabla V_p). \tag{2.5}$$

The effective potential for the holes is given by $V_p = V + U_p$. The band potential for holes U_p is negative within the active region and zero outside. The physical parameters are the (scaled) electron and hole mobilities μ_n and μ_p, respectively, and the Debye length λ, given by $\lambda^2 = \varepsilon_s U_T / q C_m L$, where ε_s is the permittivity

constant, q the elementary charge, C_m the maximal doping value, L the device diameter, and $U_T = k_B \widetilde{T}_a/q$ the thermal voltage with the Boltzmann constant k_B and the unscaled ambient (lattice) temperature $\widetilde{T}_a$. The function

$$W(n,T) = -\frac{3}{2}\,\frac{n(T-T_a)}{\tau_0}$$

in (2.2) models the energy relaxation to the equilibrium energy, where τ_0 is the energy relaxation time and $T_a = 1$ the scaled ambient (lattice) temperature.

Recombination-generation terms. The electric and optical effects are coupled through recombination-generation processes modeled by

$$R = R_{\mathrm{SRH}} + R_{\mathrm{Au}} + R_{\mathrm{spon}} + R_{\mathrm{stim}}, \tag{2.6}$$

where the first two terms denote the Shockley-Read-Hall and Auger recombination terms,

$$R_{\mathrm{SRH}}(n,p) = \frac{np - n_i^2}{\tau_p(n+n_i) + \tau_n(p+n_i)}, \quad R_{\mathrm{Au}}(n,p) = (C_n n + C_p p)(np - n_i^2), \tag{2.7}$$

with the (scaled) intrinsic density n_i and the material dependent electron and hole lifetimes τ_n and τ_p, respectively, and the Auger recombination parameters C_n and C_p. The last two recombination terms in (2.6) model recombination processes that account for the generation of photons, the spontaneous and stimulated emission[1,11]

$$R_{\mathrm{spon}}(n,p) = Bnp, \quad R_{\mathrm{stim}}(n) = \sum_m v_g g_m(n) |\Xi_m|^2 S_m, \tag{2.8}$$

respectively, where $B = \sum_m B_m$ is the material-dependent spontaneous recombination parameter, given as the sum of the parameters of all laser modes m. In the stimulated emission term, $v_g = c/\mu_{\mathrm{opt}}$ denotes the group velocity of the photons with the speed of light c and the refractive index of the material μ_{opt}. Furthermore, $g_m(n)$ denotes the optical gain, which is the amplification factor for the number of photons per unit length, $|\Xi_m|^2$ is the intensity distribution of the optical field, and S_m is the number of photons in the device. For a one-dimensional and two-dimensional modeling of the device, the number of photons has to be replaced by the number of photons in the considered cross-section of the cavity, i.e. $S_m/L_c d_c$ in the one-dimensional and S_m/L_c in the two-dimensional situation, where L_c denotes the length and d_c the width of the laser cavity.

In the following we discuss the modeling of the optical gain and the intensity distribution. The optical gain $g_m(n)$ is approximated by the common approach[1]

$$g_m(n) = g_{0,m}(n - n_{\mathrm{th}}),$$

where $g_{0,m}$ is the differential gain of the m-th mode and n_{th} is the threshold density. Assuming an undoped intrinsic region, we may assume local charge neutrality $n = p$ such that we can write $g_m(n) = g_{0,m}(p - n_{\mathrm{th}})$ in the stimulated recombination term occurring in the hole transport equations (2.5). This allows for a discretization of

the drift-diffusion equations guaranteeing positivity of the discretized hole density (see section 3.1).

The optical field intensity $|\Xi_m|^2$ for the transverse modes is computed from the solution of the waveguide equation

$$\Big(\Delta + \frac{\omega^2}{c^2}\varepsilon_{\mathrm{opt}}(n)\Big)\Xi_m = \beta_m^2 \Xi_m, \tag{2.9}$$

where β_m^2 is the corresponding eigenvalue, ω denotes the angular frequency of the emitted light, and $\varepsilon_{\mathrm{opt}}(n)$ the complex-valued dielectric function of the pumped laser averaged over one section in a longitudinal direction. It is given by $\varepsilon_{\mathrm{opt}}(n) = (\mu_{\mathrm{opt}} + ic(g_m(n) - \alpha_{\mathrm{bg}})/2\omega)^2$ (see Ref. 4). Here, $i^2 = -1$ and α_{bg} is the background absorption. The solutions of (2.9) describe the transverse modes for which the corresponding number of photons S_m is balanced by the rate equation

$$\partial_t S_m = v_g(2\mathrm{Im}(\beta_m) - \alpha_f)S_m + R_{\mathrm{spon},m}, \tag{2.10}$$

where $R_{\mathrm{spon},m} = \int_{\Omega_c} B_m np\, ds$ is the spontaneous emission rate into the mode m, Ω_c the transverse cross-section of the laser cavity, α_f the total facet loss by external output, and the modal gain $\mathrm{Im}(\beta_m)$ is the imaginary part of the eigenvalue corresponding to the solution of (2.9).

Finally, the output power of the mode m is computed by[5]

$$P_{\mathrm{out},m} = \hbar\omega v_g \alpha_f |\Xi_m|^2 S_m, \tag{2.11}$$

where $\hbar = h/2\pi$ is the reduced Planck constant.

Model simplifications. We make three simplifying assumptions. The first assumption is that the optical field is dominated by the fundamental mode so that we restrict ourselves to a single-mode laser. Thus, we only need to consider a single rate equation (2.10) and the sum in (2.8) reduces to a single term. In the following, we omit the index m.

Furthermore, the intensity distribution of the fundamental mode can be computed from the effective index approximation.[1] Here, the dielectric function is simplified by $\varepsilon_{\mathrm{opt}}(n) = \mu_{\mathrm{opt}}^2$ such that the waveguide equation can be solved explicitly in each material, assuming that the total solution is smooth and vanishes far from the active region. We will present below a comparison of the solutions obtained from the complete model including the waveguide equation and from the simplified model.

Finally, if the simplified model is considered, we approximate the modal gain $\mathrm{Im}(\beta)$, needed in the rate equation (2.10), by

$$2\mathrm{Im}(\beta) \approx \int_{\Omega_c} (g(n) - \alpha_{\mathrm{bg}})|\Xi|^2 ds. \tag{2.12}$$

The approximation (2.12) can be derived from a first-order perturbation analysis (see Ref. 1 or 25, Chapter 9) and has been also mentioned in Ref. 5.

These simplifications result in a model which is similar to the treatment of the optical field by the number of photons and the so-called confinement factor.[1,11]

However, our model allows for a local coupling of the electrical and optical effects with only slightly higher computational effort.

Scaling. We specify the scaling which leads to the above dimensionless formulation of the model equations. The spatial dimensions are scaled by the device length L; the densities n, p, n_i, and C by the maximal doping concentration $C_m = \max|C(x)|$; the electron temperature T by the ambient (lattice) temperature (usually, 300 K); the electric potential and the band potentials by the thermal voltage U_T; the mobilities μ_n and μ_p by $\bar{\mu} = \max\{\mu_n, \mu_p\}$; and the relaxation time τ_0 and the lifetimes τ_n, τ_p by $t_0 = L^2/U_T\bar{\mu}$. Furthermore, the recombination parameters C_n, C_p are scaled by $1/C_m^2 t_0$; the parameter B by $1/C_m t_0$; the group velocity v_g by L/t_0; the differential gain g_0 by $1/LC_m$; the loss parameters α_f and $\alpha_{\rm bg}$ by $1/L$; the angular frequency ω by $1/t_0$; and the number of photons S by $C_m L^3$. For notational convenience, we have not renamed the scaled quantities.

Initial and boundary conditions. The initial conditions for the transient transport equations are

$$n(\cdot,0) = n_I, \quad p(\cdot,0) = p_I, \quad T(\cdot,0) = T_I \quad \text{in } \Omega, \tag{2.13}$$

and the initial number of photons is prescribed by $S(0) = S_I$ in Ω.

The device boundary is assumed to split into two parts, the union of Ohmic contacts Γ_C and the union of insulating boundary segments Γ_I, where $\partial\Omega = \Gamma_C \cup \Gamma_I$. Although we will present below spatial one-dimensional simulations, we give the boundary conditions for the more general multi-dimensional situation. On the insulating parts, we assume that the normal components of the current densities and the electric field vanish,

$$J_n \cdot \nu = J_p \cdot \nu = J_w \cdot \nu = \nabla V \cdot \nu = 0 \quad \text{on } \Gamma_I,\ t > 0, \tag{2.14}$$

where ν is the exterior unit normal to $\partial\Omega$. At the contacts, the electric potential equals the sum of the applied voltage U and the so-called built-in potential $V_{\rm bi}$,

$$V = U + V_{\rm bi} \quad \text{on } \Gamma_C,\ t > 0. \tag{2.15}$$

The built-in potential is the potential in the device at thermal equilibrium, $V_{\rm bi} = \operatorname{arsinh}(C/2n_i)$. The temperature at the contacts fulfills homogeneous Neumann boundary conditions,

$$\frac{\partial T}{\partial \nu} = 0 \quad \text{on } \Gamma_C,\ t > 0. \tag{2.16}$$

The particle densities are assumed to fulfill boundary conditions of Robin type,

$$n + (\theta_n\mu_n)^{-1} J_n \cdot \nu = n_a \quad \text{and} \quad p - (\theta_p\mu_p)^{-1} J_p \cdot \nu = p_a \quad \text{on } \Gamma_C,\ t > 0, \tag{2.17}$$

with some parameters θ_n and θ_p. The ambient particle densities n_a and p_a are derived under the assumptions of charge neutrality, $n_a - p_a - C(x) = 0$, and thermal equilibrium, $n_a p_a = n_i^2$. Solving these equations for n_a and p_a gives

$$n_a = \frac{1}{2}\Big(C + \sqrt{C^2 + 4n_i^2}\Big), \quad p_a = \frac{1}{2}\Big(-C + \sqrt{C^2 + 4n_i^2}\Big). \tag{2.18}$$

The boundary conditions for the energy density w are derived from (2.16) and (2.17),

$$\frac{\partial w}{\partial \nu} - \theta_n(w_a - w) = \frac{3}{2}\theta_n n_a (T - T_a) + \frac{3}{2} n \frac{\partial V}{\partial \nu} \quad \text{on } \Gamma_C,\ t > 0, \tag{2.19}$$

where T_a is the (scaled) ambient temperature and w_a the ambient energy density $w_a = \frac{3}{2} n_a T_a$.

Often, (2.18) are employed as Dirichlet boundary values for the particle densities at the contacts. However, strong boundary layers for large applied voltages indicate that these boundary conditions are physically not appropriate. Therefore, we prefer to use the above Robin-type conditions which reduce the boundary layers significantly. We refer to Ref. 8 for a more detailed discussion.

For the waveguide equation (2.9), we impose the boundary condition $\Xi = 0$ on $\partial\Omega$. This coincides with the assumption that the intensity of the optical field decreases to zero at the boundary, what seems reasonable as the optical field is confined to the active region.

The total current density J_{tot} in the device is given by $J_{\text{tot}} = J_n + J_p + J_d$, where $J_d = -\lambda^2 \partial_t \nabla V$ denotes the displacement current, which guarantees charge conservation. The current leaving the semiconductor device at terminal k, corresponding to the part Γ_k of the boundary Γ_C, is then defined by $j_k = \int_{\Gamma_k} J_{\text{tot}} \cdot \nu \, ds$. Due to charge conservation, the current through one terminal can be computed by the negative sum of the currents through all other terminals. Therefore, it is possible to choose one terminal (usually the bulk terminal) as the reference terminal. For the one-dimensional examples presented below, with $\Omega = (0,1)$, there remains only one terminal, and the current through the terminal at $x = 0$ is given by

$$j_{\text{out}}(t) = J_n(0,t) + J_p(0,t) - \lambda^2 \partial_t V_x(0,t). \tag{2.20}$$

The complete model. For convenience, we summarize the complete model for a single-mode laser diode. It consists of the energy-transport equations (2.1)-(2.3) for electrons, coupled to the Poisson equation (2.4), where $V_{n/p} = V + U_{n/p}$ ($U_{n/p}$ given), the drift-diffusion model (2.5) for holes, where the recombination-generation term R is defined by (2.6)-(2.8). The sum in R_{stim} and in the spontaneous recombination parameter B reduces to a single term. In R_{stim}, the field intensity $|\Xi|^2$ is given by the waveguide equation (2.9) with $\Xi = 0$ on $\partial\Omega$ or it is simplified by the effective index approximation, and the number of photons S is computed from (2.10) with $S(0) = S_I$. The initial-boundary conditions for the parabolic equations are (2.13) and (2.14)-(2.19).

2.2. *Photo diode*

As a simplified model of a vertical photo diode, we consider a *p*-*i*-*n*-homostructure (a heterostructure could also be used) with optical irradiation at the *p*-doped contact as shown in Figure 2. The supplied light (photons) generates free charge carriers which causes the photo current.

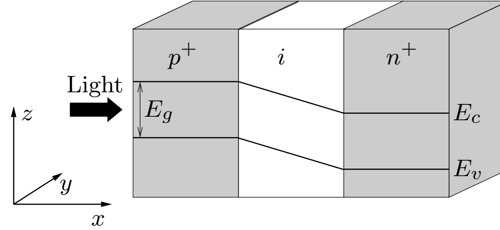

Fig. 2. Simplified structure of a silicon photo diode including a schematic illustration of the energy bands.

The transport of charge carriers is modeled by the energy-transport equations (2.1)-(2.3) for electrons, the Poisson equation (2.4), and the drift-diffusion equations (2.5) for holes. The recombination term for the photo diode is given by

$$R = R_{\text{SRH}} + R_{\text{Au}} - G_{\text{opt}}, \tag{2.21}$$

where

$$G_{\text{opt}}(x) = \eta(1-r)\frac{P_{\text{in}}}{\hbar\omega A}\alpha_{\text{ab}}e^{-\alpha_{\text{ab}}x} \tag{2.22}$$

denotes the generation rate of free charge carriers at depth x of the device caused by the optical irradiation power P_{in} with angular frequency ω.[11,17,20] The reflectivity of the surface of the diode is given by r, the optical absorption of the material by α_{ab}, the quantum efficiency (the fraction of photons that generates charge carriers) by η, and the area of the surface hit by the irradiation by A. Furthermore, $P_{\text{in}}/\hbar\omega$ is the injected number of photons per second. The current leaving the photo diode is computed according to (2.20). The boundary and initial conditions are the same as in the previous subsection. In order to couple (2.22) to the scaled energy-transport equations, we scale the power input $P_{\text{in}}/\hbar$ by L^3C_m/t_0^2, the area A by L^2 and the absorption parameter α_{ab} by $1/L$.

2.3. *Coupling the optoelectronic devices to electric circuits*

The electric circuit is modeled by the well-established modified nodal analysis (MNA). We assume that the electric circuit can be reduced to a RCL-circuit, only containing resistors, capacitors, and inductors. The basic tools for the mathematical description of RCL-circuits are the Kirchhoff laws and the current-voltage characteristics of the basic elements. In order to accomplish the MNA, the circuit is replaced by a directed graph with branches and nodes. Then, the circuit can be characterized by the incidence matrix $\mathcal{A}$ describing the node-to-branch relations.[31] The Kirchhoff laws are $\mathcal{A}i = 0$ and $v = \mathcal{A}^\top e$, where i, v, and e are the vectors of branch currents, branch voltages, and node potentials, respectively. The current-voltage characteristics read as $i_R = g(v_R)$, $i_C = dQ/dt(v_C)$, and $v_L = d\Phi/dt(i_L)$, where g denotes the conductivity of the resistor, Q the charge of the capacitor, and Φ the flux of the

inductor. Furthermore, i_α and v_α are the branch current vectors and branch voltage vectors, where $\alpha = R, C, L, i, v$ indicates the resistive, capacitive, inductive, current source, and voltage source branches, respectively. The branches can be numbered in such a way that the incidence matrix $\mathcal{A}$ can be written as block matrices $\mathcal{A}_\alpha$.

The coupling with the semiconductor device, whose position in the circuit is characterized by the incidence matrix $\mathcal{A}_S$, consists of two parts. First, the device is coupled to the surrounding circuit via the semiconductor current $j_S = j_{\text{out}}$ defined in (2.20) and entering the circuit. Denoting by $i_s(t)$ and $v_s(t)$ the input functions for the current and voltage sources, the Kirchhoff laws lead to the following system for the coupled circuit-device system in the charge-oriented nodal analysis approach,

$$\mathcal{A}_C \frac{dQ}{dt}(\mathcal{A}_C^\top e) + \mathcal{A}_R g(A_R^\top e) + \mathcal{A}_L i_L + \mathcal{A}_v i_v + \mathcal{A}_S j_S = -\mathcal{A}_i i_s, \tag{2.23}$$

$$\frac{d\Phi}{dt}(i_L) - \mathcal{A}_L^\top e = 0, \quad \mathcal{A}_v^\top e = v_s,$$

for the unknowns $e(t)$, $i_L(t)$, and $i_v(t)$, where the term $\mathcal{A}_S j_S$ entered the left-hand side of (2.23).

Second, the boundary conditions for the electric potential at the device contacts are determined by the circuit. At the terminal k connected to the circuit node i, we have $V(t) = e_i(t) + V_{\text{bi}}$, where e_i denotes the potential in the circuit node i and V_{bi} is the built-in potential defined in section 2.1.

We notice that the scaling of time in the semiconductor model also changes the time variable in the above differential-algebraic system, i.e. $t = t_0 t_s$, with scaling factor t_0 and the scaled time t_s. The time derivative d/dt changes into $t_0^{-1}(d/dt_s)$.

3. Numerical approximation

3.1. *Discretization of the differential equations*

The Poisson equation is discretized in space by linear finite elements. Thus the discrete electric potential is piecewise linear and the approximation of the electric field $-V_x$ is piecewise constant. Eqs. (2.1)-(2.10) are discretized in time by the implicit Euler method. (A discretization with the BDF2 method has lead to very similar results.) The waveguide equation (2.9) is discretized in space by standard finite elements, and the corresponding discretized eigenvalue problem is solved using the `eig` or `eigs` routine of `Matlab`.

The energy-transport equations are discretized using the mixed finite-element method. For this, we define the variables $g_1 = \mu_n n$ and $g_2 = \frac{3}{2}\mu_n n T$ and write (2.1)-(2.3) as

$$\mu_n^{-1}\partial_t g_1 - \text{div} J_n = -R(n,p), \tag{3.1}$$

$$\mu_n^{-1}\partial_t g_2 - \text{div} J_w = -J_n \cdot \nabla V_n + W(n,T) - \frac{3}{2}TR(n,p), \tag{3.2}$$

with the current densities

$$J_n = \nabla g_1 - \frac{g_1}{T}\nabla V_n, \quad J_w = \nabla g_2 - \frac{g_2}{T}\nabla V_n, \tag{3.3}$$

where the temperature now is given by $T = 2g_2/3g_1$. This corresponds (up to a sign) to the drift-diffusion equations (2.5), where p is replaced by g_1 or g_2, $T = 1$, and the right-hand sides are different. The advantage of this formulation is that it "diagonalizes" the cross-diffusion energy-transport model.[13] The initial and boundary conditions for g_1, g_2, and V follow directly from (2.14)-(2.19).

In the following, we describe the discretization of the energy-transport equations for electrons in the laser diode. The corresponding equations for holes and for the photo diode are discretized analogously. After time discretization with the implicit Euler scheme for given V, T, p, S, $|\Xi|^2$, $\widetilde{g}_1$, and $\widetilde{J}_n$ from the previous iteration step, we can express the continuity equation at time $t_{m+1} = (m+1)\Delta t$ by

$$-J_{j,x} + \sigma_j g_j = f_j, \quad J_j = g_{j,x} - \frac{g_j}{T} V_x, \quad j = 1, 2, \tag{3.4}$$

where the current densities $J_1 = J_n$ and $J_2 = J_w$ are given by (2.3) and

$$\begin{aligned}
\sigma_1 &= \widetilde{\sigma} + (\mu_n \triangle t)^{-1}, \\
\sigma_2 &= \frac{3}{2} T \widetilde{\sigma} + (\mu_n \triangle t)^{-1} + (\mu_n \tau_0)^{-1}, \\
f_1 &= \widetilde{f} + (\mu_n \triangle t)^{-1} g_1^m, \\
f_2 &= \frac{3}{2} T \widetilde{f} + (\mu_n \triangle t)^{-1} g_2^m - \widetilde{J}_n V_x + \frac{3}{2} T_a (\mu_n \tau_0)^{-1} \widetilde{g}_1.
\end{aligned}$$

Furthermore,

$$\begin{aligned}
\widetilde{\sigma} &= \mu_n^{-1} \Big(\frac{p}{\tau_p(\mu_n^{-1}\widetilde{g}_1 + n_i) + \tau_n(p + n_i)} + C_n \mu_n^{-1} \widetilde{g}_1 p + C_p p^2 + Bp + v_g g_0 |\Xi|^2 S \Big), \\
\widetilde{f} &= \frac{n_i}{\tau_p(\mu_n^{-1}\widetilde{g}_1 + n_i) + \tau_n(p + n_i)} + C_p p n_i^2 + C_n \mu_n^{-1} \widetilde{g}_1 n_i^2 + v_g g_0 n_{\mathrm{th}} |\Xi|^2 S
\end{aligned}$$

and g_j^m is the value of g_j at time step t_m.

If the zeroth-order term σ_i vanishes, the use of Raviart-Thomas finite elements in (3.4) provides a numerical scheme with a stiffness matrix which is an M-matrix, thus providing the positivity of the discrete particle density for positive boundary conditions. However, this property may not hold if $\sigma_i > 0$. Marini and Pietra[24] have developed finite elements which guarantee the positivity of the particle densities for positive Dirichlet boundary data. We will show below that this property remains valid even for the Robin boundary conditions (2.17) with $\theta_{n/p} > 0$.

Next, we describe the discretization of (3.4) in the interval $(0, 1)$ with Robin boundary conditions. For convenience, we omit the index j in (3.4). We introduce the uniform mesh $x_i = ih$, $i = 0, \ldots, N$, where $N \in \mathbb{N}$ and $h = 1/N$. In order to deal with the convection dominance due to high electric fields, we use exponential fitting. Assume in the following that the temperature is given by a piecewise constant function $\overline{T}$ (see (3.12) for the definition of $\overline{T}$) and that the electric potential V is a given piecewise linear function. Then we define a local Slotboom variable by $y = \exp(-V/\overline{T})g$ in each subinterval $I_i = (x_{i-1}, x_i)$. Eq. (3.4) can be written as

$$e^{-V/\overline{T}} J - y_x = 0, \quad -J_x + \sigma e^{V/\overline{T}} y = f \tag{3.5}$$

and the boundary conditions (2.17) transform to

$$\frac{\partial y}{\partial \nu} - \theta_n(y_a - y) = 0 \quad \text{at } x = 0, 1, \tag{3.6}$$

where $y_a = e^{-V/\overline{T}} g_a$, and $g_a = \mu_n n_a$ (see (2.18)).

The ansatz space for the current density J consists of piecewise polynomials of the form $\psi_i(x) = a_i + b_i P_i(x)$ on each I_i with constants a_i, b_i and second-order polynomials $P_i(x)$ which are defined as follows. Let $P(x) = 3x^2 - 2x$. We define $P_i(x)$ (depending on V) by

$$\begin{aligned} P_i(x) &= -P\Big(\frac{x_i - x}{h}\Big) \quad \text{for } i_{\min} = i - 1, \\ P_i(x) &= P\Big(\frac{x - x_{i-1}}{h}\Big) \quad \text{for } i_{\min} = i, \end{aligned}$$

where $i_{\min}$ is the boundary node of I_i at which the potential attains its minimum. Notice that the minimum is always attained at the boundary since V is linear on I_i. If V is constant in I_i, we define $P_i(x) = P((x - x_{i-1})/h)$.

Now we introduce as in Ref. 13 the finite-dimensional spaces

$$\begin{aligned} V_h &= \{\psi \in L^2(0,1) : \psi(x) = a_i + b_i P_i(x) \text{ in } I_i,\ i = 1, \dots, N\}, \\ W_h &= \{\phi \in L^2(0,1) : \phi \text{ is constant in } I_i,\ i = 1, \dots, N\}, \\ \Gamma_h &= \{q \text{ is defined at the nodes } x_0, \dots, x_N\}. \end{aligned}$$

The mixed-hybrid finite-element approximation of (3.5) is as follows: Find $J_h \in V_h$, $\overline{y_h} \in W_h$, and $y_h \in \Gamma_h$ such that

$$\sum_{i=1}^N \Big(\int_{I_i} Q_i J_h \psi dx + \int_{I_i} \overline{y_h} \psi_x dx - \Big[y_h \psi \Big]_{x_{i-1}}^{x_i} \Big) = 0, \tag{3.7}$$

$$\sum_{i=1}^N \Big(- \int_{I_i} J_{h,x} \phi dx + \int_{I_i} \sigma S_i^{-1} \overline{y_h} \phi dx \Big) = \sum_{i=1}^N \int_{I_i} f \phi dx, \tag{3.8}$$

$$\sum_{i=1}^N \big[q J_h \big]_{x_{i-1}}^{x_i} + q\theta_n (Q_1^{-1} y_0 + Q_N^{-1} y_N) = q\theta_n y_a (Q_1^{-1} + Q_N^{-1}), \tag{3.9}$$

for all $\psi \in V_h$, $\phi \in W_h$, and $q \in \Gamma_h$. The approximations

$$Q_i = \frac{1}{h} \int_{I_i} e^{-V(x)/\overline{T}_i} dx, \quad S_i = e^{-V_{\min}/\overline{T}_i}, \quad i = 1, \dots, N,$$

are introduced in order to treat accurately large gradients of the potential.[24] Here, $V_{\min}$ denotes the minimum value of V on I_i. Eq. (3.7) is the weak formulation of the first equation in (3.5), together with the Slotboom transformation. Eq. (3.8) is the discrete weak version of the second equation in (3.5). The third equation (3.9) expresses the weak continuity property of J_h.

The variables J_h and $\overline{y_h}$ can be eliminated by static condensation. For this, we write the weak formulation in matrix-vector notation for the vectors of nodal values

similarly as in Ref. 15:

$$\begin{pmatrix} A & B^\top & -C^\top \\ -B & D & 0 \\ C & 0 & E \end{pmatrix} \begin{pmatrix} J_h \\ \overline{y_h} \\ y_h \end{pmatrix} = \begin{pmatrix} 0 \\ F \\ G_C \end{pmatrix}.$$

The matrices $A \in \mathbb{R}^{2N\times 2N}$, $B \in \mathbb{R}^{N\times 2N}$, $C \in \mathbb{R}^{(N+1)\times 2N}$ and $D \in \mathbb{R}^{N\times N}$ are given by the corresponding elementary matrices associated with the interval I_i, denoted by the superscript i:

$$A^i_{jk} = Q_i \int_{I_i} \psi_j \psi_k dx, \qquad B^i_{jk} = \int_{I_i} \phi_j \psi_{k,x} dx,$$
$$C^i_{jk} = \left[q_j \psi_k\right]^{x_i}_{x_{i-1}}, \qquad D^i_{jk} = S_i^{-1} \int_{I_i} \sigma \phi_j \phi_k dx,$$

where ψ_k, ϕ_k, and q_k are the canonical basis functions of the corresponding spaces. In the matrix $E \in \mathbb{R}^{(N+1)\times(N+1)}$, only the values $E_{11} = q_1 q_1 \theta_n Q_1^{-1}$ and $E_{N+1,N+1} = q_{N+1} q_{N+1} \theta_n Q_N^{-1}$ are non-zero. The vectors F and G_C represent the corresponding right-hand sides of (3.8) and (3.9), respectively.

Now, static condensation can be applied.[15] As the matrix A has a diagonal structure, it can be easily inverted, which allows to eliminate J_h. A similar argument for $BA^{-1}B^\top + D$ allows to eliminate y_h. This leads to the system

$$\widetilde{M} y_h = G, \tag{3.10}$$

where M and G are given by:

$$\widetilde{M} = CA^{-1}C^\top + E - CA^{-1}B^\top(BA^{-1}B^\top + D)^{-1}BA^{-1}C^\top,$$
$$G = G_C + CA^{-1}B^\top(BA^{-1}B^\top + D)^{-1}F.$$

If only Dirichlet boundary conditions are considered, $E = 0$ and $G_C = 0$. In this case, Marini and Pietra showed that $\widetilde{M}$ is an M-matrix. If Robin boundary conditions are prescribed, we observe that the matrix E does not have any contribution to internal elements. Thus, the corresponding elementary matrices are, as in the case of Dirichlet conditions, M-matrices. If $\theta_n > 0$, the contribution of E to the boundary elementary matrices consists in nonnegative entries to the diagonal. Thus, also the boundary elementary matrices have the M-matrix property. Adding all elementary matrices shows that $\widetilde{M}$ is an M-matrix.

In order to go back to the discrete natural unknown g_h, we use a discrete inverse Slotboom transformation. Multiplying $\widetilde{M}$ column by column by $e^{V_i/\overline{T}}$, the final system for the unknown g_h becomes

$$M g_h = G. \tag{3.11}$$

Notice that M is an M-matrix since $\widetilde{M}$ does so, and thus, the positivity for the solution of (3.11) is guaranteed for positive right-hand side G. Actually, G is positive if the right-hand side f in (3.4) is positive. This is the case for the electron density equation, since the separation of the recombination terms was done in such a way

that f_1 and the zeroth-order term σ_1 are positive. An analogous discretization of the hole equations (2.5) ensures positivity for the discrete hole density as well.

The eliminated variables J_h, $\overline{y_h}$, or $\overline{g_h}$ can be computed a posteriori from the solution of (3.10) or (3.11); we refer to Ref. 16 and Ref. 24 for the corresponding formulas. In order to complete the scheme, we still have to specify how the piecewise constant temperature $\overline{T}$ is defined. The temperature is implicitly defined in terms of g_1 and g_2, $T = 2g_2/3g_1$. Hence, we set

$$\overline{T}_i = \frac{1}{2}(T_i + T_{i-1}), \quad \text{where } T_i = \frac{2g^i_{2,h}}{3g^i_{1,h}}. \tag{3.12}$$

3.2. *Iterative scheme*

The discrete system is solved by a variant of the Gummel scheme employed for the solution of the stationary energy-transport model.[15,16] To solve the model equations for the laser diode at time $t_{m+1} = (m+1)\triangle t$, we take as initial values of the iteration the solution of the previous time step, $g_1^{(0)} = \widetilde{g}_1$, $g_2^{(0)} = \widetilde{g}_2$, $p^{(0)} = \widetilde{p}$, $V^{(0)} = \widetilde{V}$, $S^{(0)} = \widetilde{S}$, $\Xi^{(0)} = \widetilde{\Xi}$, and $\beta^{(0)} = \widetilde{\beta}$, here denoted with a tilde. Notice that in the one-dimensional situation, $\partial\Omega = \Gamma_C = \{0,1\}$. We set $g_{1,a} = \mu_n n_a$ and $g_{2,a} = \frac{3}{2}\mu_n n_a T_a$. The iterative procedure for the laser diode reads as follows:

(1) Let $\ell \in \mathbb{N}_0$ and $p^\star = p^{(\ell)}$, $g_1^\star = g_1^{(\ell)}$, $V = V^{(\ell)}$.
(2) Find S such that

$$S\big(1 - \triangle t v_g(2\mathrm{Im}(\beta^{(\ell)}) - \alpha_f)\big) = \widetilde{S}B\mu_n^{-1}g_1^\star p^\star \triangle t. \tag{3.13}$$

(3) Do
  (a) Set $V_n = V + U_n$ and find g_1 such that

$$\begin{cases} -\mathrm{div}J_1 + \sigma_1(p^\star, g_1^\star, \Xi^{(\ell)}, S, \triangle t)g_1 = f_1(p^\star, g_1^\star, \Xi^{(\ell)}, S, \triangle t, \widetilde{g}_1) & \text{in } \Omega, \\ J_1 = \nabla g_1 - \nabla V_n \overline{T}^{-1} g_1 & \text{in } \Omega, \\ g_1 + \theta_n^{-1} J_1 \cdot \nu(x) = g_{1,a} & \text{on } \Gamma_C; \end{cases} \tag{3.14}$$

  (b) Set $V_p = V + U_p$ and find p such that

$$\begin{cases} -\mathrm{div}J_p + \sigma_p(p^\star, g_1^\star, \Xi^{(\ell)}, S, \triangle t)g_1 = f_p(p^\star, g_1^\star, \Xi^{(\ell)}, S, \Delta t, \widetilde{p}) & \text{in } \Omega, \\ J_p = -\nabla p - \nabla V_p p & \text{in } \Omega, \\ p - (\theta_p\mu_p)^{-1} J_p \cdot \nu(x) = p_a & \text{on } \Gamma_C; \end{cases} \tag{3.15}$$

  (c) Set $n = \mu_n^{-1} g_1$ and $V_1 = V + \delta V$, where δV is the solution of

$$\begin{cases} \lambda^2\Delta(\delta V) - (p+n)\delta V = -\lambda^2\Delta V + n - p - C & \text{in } \Omega, \\ \delta V = 0 & \text{on } \Gamma_C; \end{cases} \tag{3.16}$$

  (d) Set $g_1^\star := g_1, p^\star := p$, and $V := V_1$;

  until $\|\delta V\|_{L^2} < \min(\mathrm{tol}_{\mathrm{int}}, d_1(\delta T)^{d_2})$, where δT is defined in step (5).

(4) Set $V_n = V + U_n$ and find g_2 such that

$$\begin{cases} -\mathrm{div} J_2 + \sigma_2(p^\star, g_1^\star, \Xi^{(\ell)}, S, \triangle t) g_2 = f_2(p^\star, g_1^\star, \Xi^{(\ell)}, S, \Delta t, \widetilde{g}_2) & \text{in } \Omega, \\ J_2 = \nabla g_2 - \nabla V_n \overline{T}^{-1} g_2 & \text{in } \Omega, \\ \frac{\partial g_2}{\partial \nu} - \theta_n (g_{2,a} - g_2) = \frac{3}{2} \theta_n g_{1,a} (\overline{T} - T_a) + \frac{3}{2} g_1 \nabla V \cdot \nu(x) & \text{on } \Gamma_C; \end{cases} \tag{3.17}$$

(5) Compute $\overline{T} = 2g_2/3g_1$ and $\delta T = \|\overline{T} - T_a\|_{L^2}$.
(6) Define $V^{(\ell+1)} = V + \delta V$, where δV is the solution of (3.16).
(7) Find $\Xi^{(\ell+1)}$ and $\beta^{(\ell+1)}$ such that

$$\begin{cases} \left(\Delta + \frac{\omega^2}{c^2} \varepsilon_{\mathrm{opt}}\right) \Xi^{(\ell+1)} = (\beta^{(\ell+1)})^2 \Xi^{(\ell+1)} & \text{in } \Omega, \\ \Xi^{(\ell+1)} = 0 & \text{on } \Gamma_C. \end{cases} \tag{3.18}$$

(8) Set $g_1^{(\ell+1)} := g_1$, $g_2^{(\ell+1)} := g_2$, $p^{(\ell+1)} := p$, and $T^{(\ell+1)} := \overline{T}$.

We stop the iteration procedure if the relative difference of two consecutive iterations of $(g_1^{(\ell)}, g_2^{(\ell)}, p^{(\ell)}, T^{(\ell)})$, $(S^{(\ell)}, \Xi^{(\ell)})$ are smaller in the L^2-norm than the tolerances $\mathrm{tol}_{\mathrm{el}}$ and $\mathrm{tol}_{\mathrm{op}}$, respectively. The described iterative scheme performs best for $\mathrm{tol}_{\mathrm{int}} = 10^{-6}$, $d_1 = 10^{-4}$, and $d_2 = 0.3$. Moreover, we have taken $\mathrm{tol}_{\mathrm{el}} = \mathrm{tol}_{\mathrm{op}} = 10^{-5}$. The boundary layers can be significantly reduced if we take $\theta_n = \theta_p = 2500$.

The discretization (3.13) makes necessary to impose the restriction $\triangle t < 1/v_g(2\mathrm{Im}(\beta^{(\ell)}) - \alpha_f)$ on the time step to ensure the positivity of S. The choice $\triangle t = 10^{-12}\,\mathrm{s}$ proved to be appropriate for all presented simulations.

To achieve convergence when the applied voltage between two time steps changes abruptly (e.g. digital signal) or for stationary computations, the above iterative scheme is embedded in a continuation method for the applied bias:

Do

(1) Apply the iterative algorithm for the applied voltage $\widetilde{V}_a = V_{a,\mathrm{old}} + \triangle V$ until the tolerance or the maximum number of iterations is reached. As an initial guess for all variables, the values from the former voltage step are used;
(2) If the tolerance is achieved, set $V_{a,\mathrm{old}} = \widetilde{V}_a$, otherwise decrease the voltage step size $\triangle V := \triangle V/2$;

until $\widetilde{V}_a = U$.

In the simulations, we have taken $\triangle V = 0.1\,\mathrm{V}$.

For the simulation of the photo diode, the iterative algorithm changes slightly. The solution of the rate equation (3.13) and the solution of the waveguide equation (3.18) become obsolete. The remaining algorithm differs only slightly from that one proposed in Ref. 15 and 16. For high optical irradiation or strong changes in the irradiation (in the transient simulation), we applied a continuation method in the irradiation similar to that for the applied bias.

The output current is used as an input of the electric circuit. Then the DAE system is solved by the Newton method and the output, the node potentials, are

employed as an input for the energy-transport system, and the output current is computed. This procedure is repeated until the difference of two successive iterations is sufficiently small.

4. Numerical examples

4.1. *Characteristics of the laser diode*

We consider a GaAs/$Al_{0.7}Ga_{0.3}As$ p-i-n laser diode under various bias conditions. The one-dimensional diode has the length $1\,\mu$m consisting of a p-doped part with length $0.45\,\mu$m, a low-doped (intrinsic) part with length $0.1\,\mu$m, and an n-doped region with length $0.45\,\mu$m. The doping concentrations are $-10^{24}\,\mathrm{m}^{-3}$ in the p-doped, $10^{18}\,\mathrm{m}^{-3}$ in the low-doped region, and $10^{24}\,\mathrm{m}^{-3}$ in the n-doped part. The doping profile is slightly smoothed by use of the tanh function.[19] The band potential, consisting of the constant values $U_{n,0}$, $U_{p,0}$, respectively, in the active region and zero elsewhere, is also slightly smoothed. The values for $U_{n,0}$ and $U_{p,0}$ are rough approximations according to the contact potential computations in Ref. 11. The remaining physical parameters for the diode are collected in Table 1. For the computations we have employed a uniform spatial grid with 101 nodes and a time step size of 1 ps.

Parameter	Physical meaning	Numerical value
L_y	extension of the device in y-direction	10^{-6} m
L_z	extension in z-direction	10^{-5} m
q	elementary charge	$1.6 \cdot 10^{-19}$ As
U_T	thermal voltage at 300 K	0.026 V
$U_{n,0}/U_{p,0}$	band potentials in active region	$0.1/-0.1$ V
C_n/C_p	Auger recombination parameters[22]	$10^{-43}/10^{-42}\,\mathrm{m^6 s^{-1}}$
B	spontaneous recombination parameter[1]	$10^{-16}\,\mathrm{m^3 s^{-1}}$
τ_n/τ_p	carrier lifetimes[22]	$10^{-6}/10^{-5}$ s
τ_0	energy relaxation time[13]	$4 \cdot 10^{-13}$ s
n_{th}	threshold density[1]	$10^{24}\,\mathrm{m}^{-3}$
α_{bg}	optical background loss[1]	$4000\,\mathrm{m}^{-1}$
α_f	facet loss[1]	$5000\,\mathrm{m}^{-1}$
ϵ_0	permittivity constant[22]	$8.85 \cdot 10^{-12}\,\mathrm{As(Vm)^{-1}}$
$\epsilon_s^A/\epsilon_s^G$	material permittivity[22]	$12.1 \cdot \epsilon_0/12.9 \cdot \epsilon_0$
μ_n^A/μ_n^G	electron mobilities[22]	$2300/8300\,\mathrm{cm^2(Vs)^{-1}}$
μ_p^A/μ_p^G	hole mobilities[22]	$145/400\,\mathrm{cm^2(Vs)^{-1}}$
$\mu_{\mathrm{opt}}^A/\mu_{\mathrm{opt}}^G$	refractive index[22]	3.3/3.15
n_i^A/n_i^G	intrinsic density[22]	$2.1 \cdot 10^9/2.1 \cdot 10^{12}\,\mathrm{m}^{-3}$
g_0^G	differential gain in GaAs (see Refs. 1, 9)	$3 \cdot 10^{-21}\,\mathrm{m}^2$
ω	angular frequency (wave length 870 nm)	$2.17 \cdot 10^{-15}$ Hz

Table 1. Physical parameters for a laser diode of $Al_{0.7}Ga_{0.3}As$ and GaAs. The parameters with superscript A denote the values for $Al_{0.7}Ga_{0.3}As$, and those with superscript G denote the values for GaAs. The parameters without superscript are valid for both materials.

First we consider the response of the laser diode to various voltage signals computed with the complete model including the waveguide equation or with the simplified model in which the effective index approximation has been applied. For the transient simulations, we assume that the device is initially in thermal equilibrium without any optical field. The initial conditions are thus

$$g_1 = \mu_n e^{-V_{\mathrm{eq}}}, \quad g_2 = \frac{3}{2}\mu_n n_{\mathrm{eq}}, \quad p = e^{V_{\mathrm{eq}}}, \quad V = V_{\mathrm{eq}}, \quad T = 1, \quad S = 0$$

at time $t = 0$, where V_{eq} is the thermal equilibrium potential given by

$$\lambda^2 V_{\mathrm{eq},xx} = e^{-V_{\mathrm{eq}}} - e^{V_{\mathrm{eq}}} - C(x) \quad \text{in } (0,1), \quad V_{\mathrm{eq}}(0) = V_{\mathrm{bi}}(0), \quad V_{\mathrm{eq}}(1) = V_{\mathrm{bi}}(1).$$

Recall that V_{bi} is the built-in potential defined in section 2.1.

The laser diode is biased with a sinusoidal signal with amplitudes 2 V and 3 V and frequency 1 GHz. In Figure 3 the modal gain $2\mathrm{Im}(\beta)$ computed from (2.9) is compared with the approximation (2.12) during one oscillation of the input signal. The signal exceeds the threshold voltage for about $0.4\,\mathrm{ps} \le t \le 0.6\,\mathrm{ps}$. We see that the simplified model well approximates the modal gain, even for larger applied voltage. Below the threshold voltage, both modal gains coincide with the background loss. Figure 4 shows the intensity distribution $|\Xi|^2$ of the optical field at time $t = 5 \cdot 10^{-9}\,\mathrm{s}$. The approximated intensity distribution agrees very well with the intensity distribution computed from the complete model. These results motivate the use of the simplified model for the following simulations.

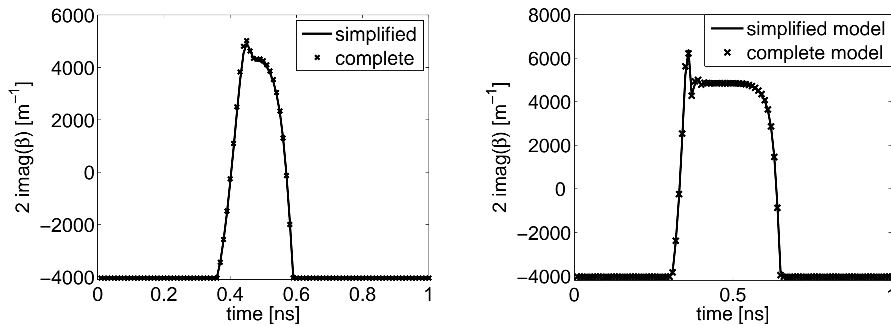

Fig. 3. Laser diode biased with a sinusoidal signal $U_0 \sin(2\pi 10^9\,\mathrm{Hz}\,t)$. Comparison of the modal gain $2\mathrm{Imag}(\beta)$ during one oscillation computed from the complete and the simplified model with applied bias of $U_0 = 2\,\mathrm{V}$ (left) and $U_0 = 3\,\mathrm{V}$ (right).

In Figure 5 the output signal is presented for various applied voltages and the (transient) drift-diffusion (DD) and energy-transport (ET) models. The left figure shows the optical output power from a sinusoidal signal with 1 GHz. The overshoot of the energy-transport model at about $t = 0.4\,\mathrm{ns}$ is caused by the transient response

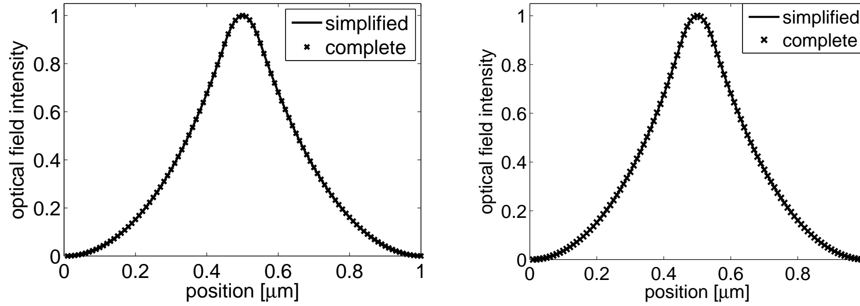

Fig. 4. Laser diode biased with a sinusoidal signal $U_0 \sin(2\pi 10^9\,\mathrm{Hz}\,t)$. Intensity distribution of the optical field at the maximum bias of $U_0 = 2\,\mathrm{V}$ (left) and $U_0 = 3\,\mathrm{V}$ (right).

of the device. The differences between the drift-diffusion and energy-transport models become more significant at larger applied voltage as seen in the right figure for a digital signal. This is expected since the energy-transport equations includes thermal effects.

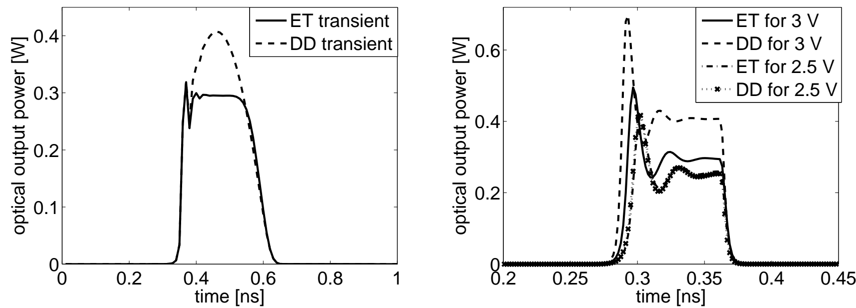

Fig. 5. Response of the laser diode to the sinusoidal input signal $3\sin(2\pi 10^9\,\mathrm{Hz}\,t)\,\mathrm{V}$ (left) and to the digital input signal with frequency 5 GHz and duration 100 ps.

Next, we present the steady characteristics of the laser diode (Figure 6). The left figure shows a current saturation in case of the energy-transport model. This behavior cannot be observed for the drift-diffusion model as the mobility μ_n is assumed to be constant and hence, the drift $-\mu_n V_x$ is unbounded in the electric field. When the relaxation time becomes smaller, the characteristics seem to converge to the curve of the drift-diffusion model. This can be understood from the fact that a vanishing relaxation time forces the particle temperature to relax to the constant ambient (lattice) temperature. The power-current characteristics are shown in the right figure. For both models we observe the presence of a threshold current of about

8 mA and an approximate linear behavior for currents between 0.1 A and 0.3 A. The output power computed from the drift-diffusion model is linearly increasing even for larger currents. For the energy-transport model, however, the output power diminishes for large currents. A similar effect has been observed in Ref. 5 using the drift-diffusion model for higher lattice temperatures (also see Ref. 1, Chap. 7). This may indicate the importance of including thermal effects.

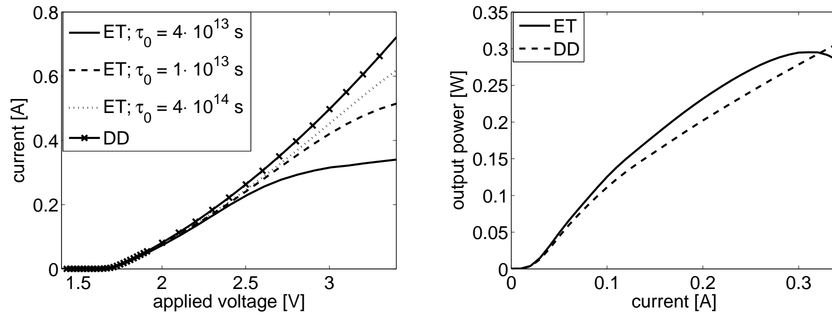

Fig. 6. Characteristics of the laser diode using the drift-diffusion and energy transport models with different relaxation times. Left: Current-voltage characteristics. Right: Power-current characteristics.

Finally, Figure 7 shows the stationary electron density and temperature in the device for two different forward bias. We clearly see the carrier confinement in the active region. Hot electrons are present mainly in the p-doped region and the temperature becomes minimal at the p-i heterojunction. This minimum is a well known thermoelectric effect at p-n junctions.[26] For larger applied bias, the electron temperature becomes large also in the n-doped region.

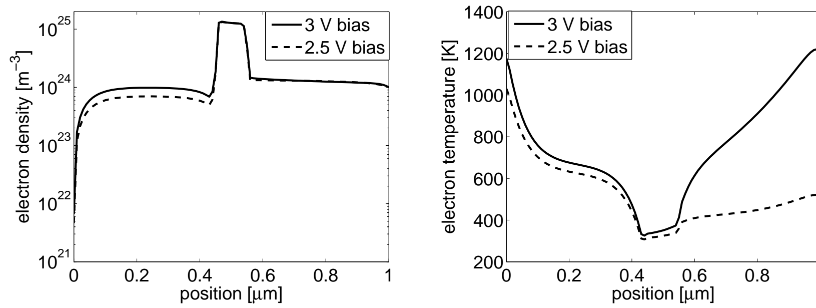

Fig. 7. Electron density (left) and electron temperature (right) in the laser diode for different forward bias.

Parameter	Physical meaning	Numerical value
L_y	extension of device in y-direction	10^{-5} m
L_z	extension in z-direction	10^{-4} m
q	elementary charge	$1.6 \cdot 10^{-19}$ As
ϵ_s	permittivity constant[22]	10^{-10} As(Vm)$^{-1}$
U_T	thermal voltage at 300 K	0.026 V
μ_n/μ_p	low-field carrier mobilities[22]	1500/450 cm^2(Vs)$^{-1}$
τ_n/τ_p	carrier lifetimes[22]	$10^{-6}/10^{-5}$ s
n_i	intrinsic density[22]	10^{16} m^{-3}
τ_0	energy relaxation time[13]	$4 \cdot 10^{-13}$ s
η	quantum efficiency	0.5
r	surface reflectivity	0.3
α_{ab}	absorption	5000 m^{-1}

Table 2. Physical parameters for a silicon p-i-n-junction diode.

4.2. *Photo diode*

The one-dimensional vertical silicon p-i-n photo diode has the length 6 μm consisting of a p-doped part of 2 μm length doped with $-5 \cdot 10^{22}$ m^{-3}, an intrinsic region of 2μm length doped with $5 \cdot 10^{17}$m^{-3}, and an n-doped region of length 2 μm doped with $5 \cdot 10^{22}$m^{-3}. Again, the doping profile is slightly smoothed. The physical parameters for the diode are listed in Table 2. The geometry of the device is similar to that of Ref. 29. For the following numerical tests we employ a uniform grid with 101 nodes and the time step 5 ps.

In Figure 8 the dark current (no irradiation) and the photo current (positive irradiation) under backward bias are presented. The current increases significantly with increasing irradiation, proving that our model well reflects the typical behavior of a photo diode.

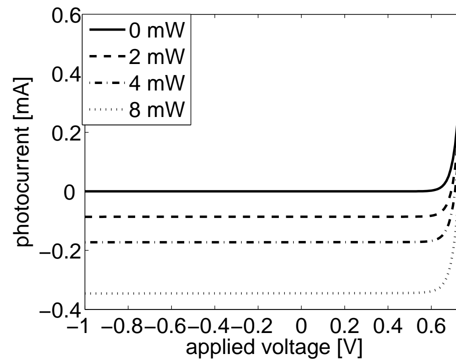

Fig. 8. Dark current and photo current in the photo diode for various irradiation intensity.

In the following numerical tests, the diode is driven by the backward bias of 0.2 V. The response of the device to a sinusoidal irradiation signal with amplitude 60 mW and frequency 1 GHz and to a digital signal with duration 200 ps are shown in Figure 9. We observe that the stationary energy-transport model does not give satisfactory results. The numerical results of the drift-diffusion and the energy-transport models are similar since the photo currents are rather small.

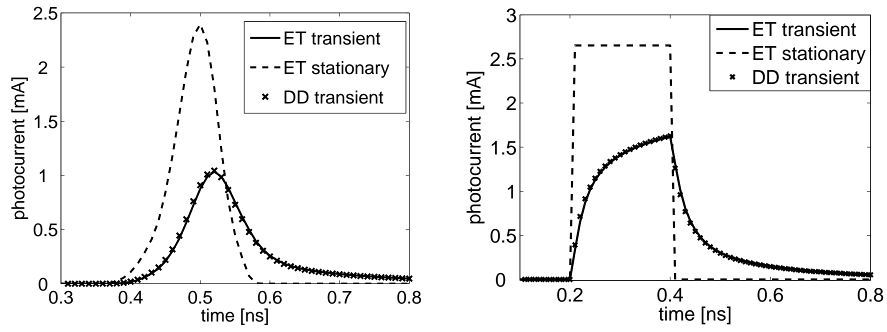

Fig. 9. Response of the photo diode under backward bias of 0.2V for various irradiation signals. Left: Sinusoidal signal $P(t) = 60 \sin(2\pi 10^9 \,\mathrm{Hz}\, t)$ mW. Right: Digital signal with amplitude 60 mW and duration 200 ps.

The stationary electron energy density and temperature are presented in Figure 10. The energy density (left figure) strongly increases in the p-doped and intrinsic regions with increasing irradiation. This is mainly caused by the increase of photo electrons in these regions since the temperature only increases in the intrinsic part of the device.

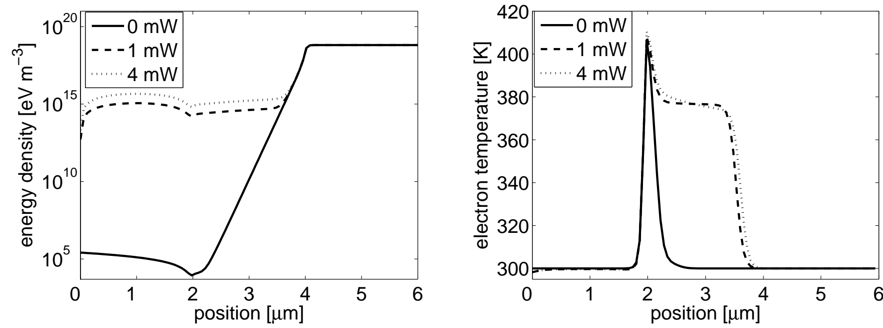

Fig. 10. Electron energy density (left) and temperature (right) in the photo diode under backward bias of 0.2 V for various irradiation power.

4.3. *High-pass filter including optoelectronic devices*

In this subsection we consider the laser and photo diode as part of a small electric circuit (see Figure 11). The laser diode is biased with a digital input signal with bias of 2.5 V and 3 V with frequencies 1 GHz and 5 GHz. The photo diode receives the transmitted signal and is coupled to a high-pass filter only passing frequencies larger than the cutoff frequency. The filter consists of the photo diode, a capacitor, and three resistors. The capacitance is 10 pF and the resistances are $R_1 = 1\,\mathrm{M}\Omega$ and $R_2 = 100\,\Omega$. For the load resistance, we have chosen $R_L = 1\,\mathrm{k}\Omega$. The photo diode is backward biased with 0.2 V.

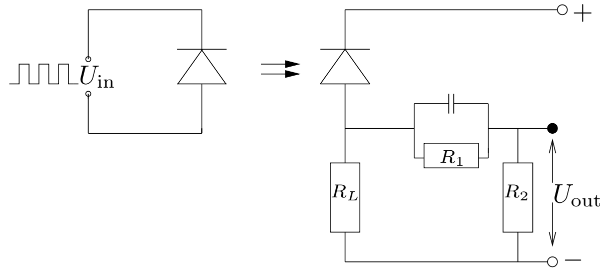

Fig. 11. Photo diode with a high-pass filter.

The output of the laser diode (which is the input for the photo diode) and the high-pass filter for a 2.5 V digital signal U_{in} is shown in Figure 12 (upper row) for stationary and transient device simulations. The results for the high-pass output voltage differ significantly as the frequency is too large to be resolved by the stationary model. On the other hand, the differences between the drift-diffusion and the energy-transport equations are minor. This behavior changes drastically when the digital signal becomes larger. Figure 12 (lower row) shows the output of the laser diode and the high-pass filter for a digital signal of 3 V. The output from the drift-diffusion model is larger than that from the energy-transport equations.

The effect of a larger frequency is shown in Figure 13. We have employed a digital signal with a five times larger frequency than that of Figure 12. Again, the large frequency cannot be resolved by the stationary model.

In order to verify the filter effect, we apply digital signals with 2.5 V bias with various frequencies using the stationary energy-transport model (Figure 14). The use of the stationary model is justified by the chosen frequencies and applied voltage. The numerical results show that only high frequencies provide a significant output signal showing the high-pass behavior.

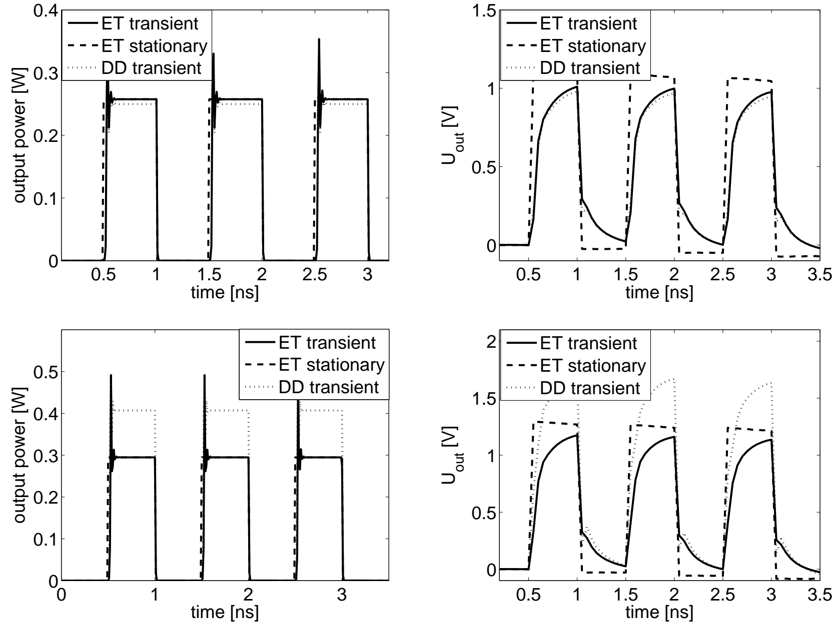

Fig. 12. Output of the laser diode (left) and the high-pass filter (right) computed from the drift-diffusion and energy-transport models for a 1 GHz digital input signal with bias 2.5 V (upper row) and 3 V (lower row).

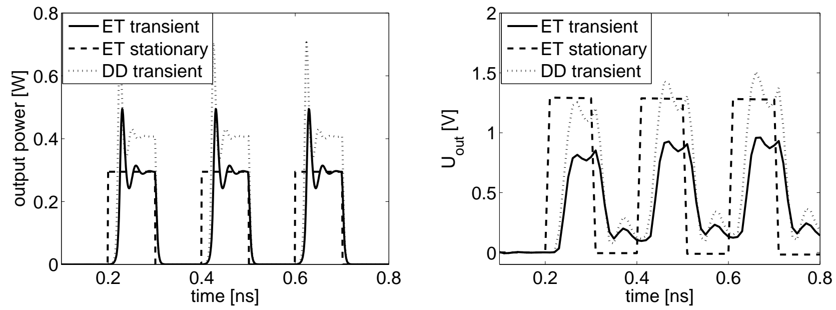

Fig. 13. Output of the laser diode (left) and the high-pass filter (right) computed from the drift-diffusion and energy-transport models for a 5 GHz digital input signal with bias 3 V.

5. Conclusion

In this paper, we have presented a coupled optoelectronic device-circuit model based on the energy-transport equations. The model becomes a system of nonlinear partial differential-algebraic equations. The mixed finite-element scheme with Marini-

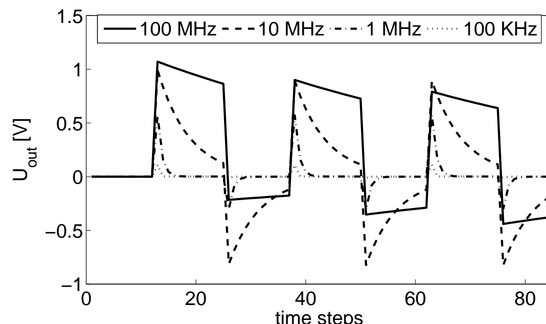

Fig. 14. Output of the high-pass filter for input signals of various frequencies.

Pietra elements is proven to be positivity-preserving also for Robin boundary conditions.

The numerical results for a single-mode laser diode and a photo diode show that the basic behavior of the devices can be reproduced by our model. For large applied voltages, the drift-diffusion and energy-transport model give significantly different results due to thermal effects. For small frequencies, the stationary energy-transport model is sufficient but for higher frequencies, the transient model has to be employed. The photo diode has been coupled to a high-pass filter which takes the laser diode output as an input for the circuit. The simulations clearly show the filter effect.

The numerical results indicate that thermal effects play an important role in circuits with large applied bias. In these situations it is expected that the energy-transport model gives better results than the drift-diffusion equations. In future simulations, we intend to include an equation for the device temperature coupled to the electron temperature.

References

1. G. P. Agrawal and N. K. Dutta. *Semiconductor Lasers.* Second Edition. Van Nostrand Reinhold, New York, 1993.
2. G. Alì, A. Bartel, and M. Günther. Parabolic differential-algebraic models in electric network design. *SIAM Multiscale Model. Simul.* 4 (2005), 813-838.
3. P. S. André, P. Antunes, A. L. J. Teixeira, and J. L. Pinto. Simplified heat exchange model for semiconductor laser diodes thermal parameters extraction. *Laser Phys. Lett.* 2 (2005), 525-528.
4. U. Bandelow, R. Hünlich, and T. Koprucki. Simulation of static and dynamic properties of edge-emitting multiple-quantum-well lasers. *IEEE J. Selected Topics Quantum Electr.* 9 (2003), 798-806.
5. U. Bandelow, H. Gajewski, and R. Hünlich. Fabry-Perot Lasers: thermodynamics-based modeling. In: J. Piprek (ed.), *Optoelectronic Devices. Advanced Simulation and Analysis.* Springer, Berlin (2005), 63-85.
6. U. Bandelow, M. Radziunas, V. Z. Tronciu, H. J. Wünsche, and F. Henneberger.

Tailoring the dynamics of diode lasers by passive dispersive reflectors. In: R. H. Binder et al. (eds.), *Physics and Simulation of Optoelectronic Devices VIII.* Proceedings of SPIE 3944, (2000), 536-545.
7. N. Ben Abdallah and P. Degond. On a hierarchy of macroscopic models for semiconductors. *J. Math. Phys.* 37 (1996), 3308-3333.
8. M. Brunk and A. Jüngel. *Numerical coupling of electric circuit equations and energy-transport models for semiconductors*. To appear in *SIAM J. Sci. Comput.*, 2007.
9. P. A. Chen, C. Y. Chang, and C. Juang. Analysis of differential gain in GaAs/AlGaAs quantum well lasers. *J. Appl. Phys.* 76 (1994), 85-91.
10. W. W. Chow, S. W. Kochm, and M. Sargent III. *Semiconductor-Laser Physics.* Springer, 1997.
11. S. L. Chuang. *Physics of Optoelectronic Devices.* Wiley, New York, 1995.
12. Crosslight Software Inc. *Crosslight Device Simulation Software Information.* www.crosslight.com, 2005.
13. P. Degond, A. Jüngel, and P. Pietra. Numerical discretization of energy-transport models for semiconductors with non-parabolic band structure. *SIAM J. Sci. Comput.* 22 (2000), 986-1007.
14. A. Gilg and M. Günther. Numerical circuit simulation. *Surv. Math. Ind.* 8 (1999), 165-169.
15. S. Holst, A. Jüngel, and P. Pietra. A mixed finite-element discretization of the energy-transport equations for semiconductors. *SIAM J. Sci. Comput.* 24 (2003), 2058-2075.
16. S. Holst, A. Jüngel, and P. Pietra. An adaptive mixed scheme for energy-transport simulations of field-effect transistors. *SIAM J. Sci. Comput.* 25 (2004), 1698-1716.
17. G. R. Jones, R. J. Jones, and W. French. Infrared HgCdTe Optical Detectors. In: J. Piprek (ed.), *Optoelectronic Devices. Advanced Simulation and Analysis.* Springer, Berlin (2005), 381-403.
18. A. Jüngel. *Quasi-hydrodynamic Semiconductor Equations*. Birkhäuser, Basel, 2001.
19. A. Jüngel and S. Tang. Numerical approximation of the viscous quantum hydrodynamic model for semiconductors. *Appl. Numer. Math.* 56 (2006), 899-915.
20. K. Konno, O. Matsushima, D. Navarro, and M. Miura-Mattausch. High frequency response of *p-i-n* photodiodes analyzed by an analytical model in Fourier space. *J. Appl. Phys.* 96 (2004), 3839-3844.
21. N. Korneyev, M. Radžiūnas, H. J. Wünsche, and F. Henneberger. Mutually injecting semiconductor lasers: simulations for short and zero delay. In: D. Lenstra et al. (eds.), *Semiconductor Lasers and Laser Dynamics.* Proceedings of SPIE 5452 (2004), 63-70.
22. M. E. Levinshtein. *Handbook Series on Semiconductor Parameters.* World Scientific, London, 1996.
23. W. Li, X. Li, and W.-P. Huang. A traveling-wave model of laser diodes with consideration for thermal effects. *Optical Quantum Electr.* 36 (2004), 709-724.
24. L. D. Marini and P. Pietra. New mixed finite element schemes for current continuity equations. *COMPEL* 9 (1990), 257-268.
25. P. M. Morse and H. Feshbach. *Methods of Theoretical Physics.* McGraw-Hill, New York, 1953.
26. K. Pipe, R. Ram, and A. Shakouri. Bias-dependent Peltier coefficient and internal heating in bipolar devices. *Phys. Rev. B* 66 (2002), 125316.
27. J. Piprek. *Semiconductor Optoelectronic Devices: Introduction to Physics and Simulation.* Academic Press, New York, 2003.
28. M. Selva Soto and C. Tischendorf. Numerical analysis of DAEs from coupled circuit and semiconductor simulation. *Appl. Numer. Math.* 53 (2005), 471-488.
29. G. Suzuki, K. Konno, D. Navarro, N. Sadachika, Y. Mizukane, O. Matsushima, and

M. Miura-Mattausch. Time-domain-based modeling of carrier transport in lateral p-i-n photodiode. *Proceedings of the International Conference of Semiconductor Processes and Devices (SISPAD 2005)*, 107-110.

30. T. N. Swe and K. S. Yeo. An accurate photodiode model for DC and high frequency SPICE circuit simulation. In: *Technical Proceedings of the 2001 International Conference on Modeling and Simulation of Microsystems*, Nanotech 2001 Vol. 1 (2001), 362-365.
31. C. Tischendorf. Modeling circuit systems coupled with distributed semiconductor equations. In: K. Antreich, R. Bulirsch, A. Gilg, and P. Rentrop (eds.), *Modeling, Simulation, and Optimization of Integrated Circuits*. Int. Series Numer. Math. 146 (2003), 229-247.
32. P. Wen, M. Sanchez, M. Gross, O. Kibar, and S. C. Esener. New photon density rate equation for Fabry-Perot semiconductor optical amplifiers (FP SOAs). In: P. Blood et al. (eds.), *Physics and Simulation of Optoelectronic Devices X*. Proceedings of SPIE 4646 (2002), 243-250.